Journal of Rock Mechanics and Geotechnical Engineering 14 (2022) 1253–1265

Contents lists available at ScienceDirect

Journal of Rock Mechanics and Geotechnical Engineering

journal homepage: www.jrmge.cn

Full Length Article

A stable CS-FEM for the static and seismic stability of a single square tunnel in the soil where the shear strength increases linearly with depth

H.C. Nguyen [a,b,*], L. Nguyen-Son [c]

[a] Department of Civil and Environmental Engineering, Imperial College London, London, UK
[b] Department of Civil Engineering and Industrial Design, University of Liverpool, Liverpool, UK
[c] Faculty of Civil Engineering, Ho Chi Minh City University of Technology (HUTECH), Ho Chi Minh City, Viet Nam

ARTICLE INFO

Article history:
Received 3 June 2021
Received in revised form
18 November 2021
Accepted 20 January 2022
Available online 14 March 2022

Keywords:
Tunnels
Stability
Limit analysis
Cell-based smoothed finite element method (CS-FEM)
Second-order cone programming (SOCP)

ABSTRACT

A numerical procedure using a stable cell-based smoothed finite element method (CS-FEM) is presented for estimation of stability of a square tunnel in the soil where the shear strength increases linearly with depth. The kinematically admissible displacement fields are approximated by uniform quadrilateral elements in conjunction with the strain smoothing technique, eliminating volumetric locking issues and the singularity associated with the Mohr–Coulomb model. First, a rich set of simulations was performed to compute the static stability of a square tunnel with different geometries and soil conditions. The presented results are in excellent agreement with the upper and lower bound solutions using the standard finite element method (FEM). The stability charts and tables are given for practical use in the tunnel design, along with a newly proposed formulation for predicting the undrained stability of a single square tunnel. Second, the seismic stability number was computed using the present numerical approach. Numerical results reveal that the seismic stability number reduces with an increasing value of the horizontal seismic acceleration (α_h), for both cases of the weightless soil and the soil with unit weight. Third, the link between the static and seismic stability numbers is described using corrective factors that represent reductions in the tunnel stability due to seismic loadings. It is shown from the numerical results that the corrective factor becomes larger as the unit weight of soil mass increases; however, the degree of the reduction in seismic stability number tends to reduce for the case of the homogeneous soil. Furthermore, this advanced numerical procedure is straightforward to extend to three-dimensional (3D) limit analysis and is readily applicable for the calculation of the stability of tunnels in highly anisotropic and heterogeneous soils which are often encountered in practice.

1. Introduction

In this paper, we present a cell-based smoothed finite element method (CS-FEM) to estimate the static and seismic stability of a square tunnel in the soil where the shear strength varies with depth in a linearly increasing manner. Sloan and Assadi (1991) presented two numerical procedures using finite element formulations of the classic lower and upper bound theorems to calculate the rigorous bounds on the undrained stability of a square tunnel. The loads to resist the collapse (Sloan and Assadi, 1991) were solved by optimizations established in large sparse linear programming problems (LNP) using limit theorems. An extension to the establishment of optimizations of two bounds in a conic form was outlined by Wilson et al. (2013), along with the use of rigid-block upper bound method to predict the undrained stability of the square tunnel. The solutions to the undrained stability of a square tunnel were improved significantly, with upper and lower bound solutions to the collapse load in a range of 5%. Recently, Vo-Minh and Nguyen-Son (2021) presented an upper bound limit analysis using the node-based smoothed finite element to calculate the stability of two circular tunnels at different depths in cohesive-frictional soils, with very satisfactory results. It was reported by Meng et al. (2020) and Nguyen and Vo-Minh (2022a) that such a low-order mixed element can overcome the volumetric locking problems as well as the singularity associated with the Mohr–Coulomb model. More recently, Nguyen and Vo-Minh (2022b)

* Corresponding author. Department of Civil and Environmental Engineering, Imperial College London, London, UK.
E-mail addresses: h.nguyen15@imperial.ac.uk, H.C.Nguyen@liverpool.ac.uk (H.C. Nguyen).
Peer review under responsibility of Institute of Rock and Soil Mechanics, Chinese Academy of Sciences.

https://doi.org/10.1016/j.jrmge.2022.01.006

confirmed that the use of the strain smoothing technique in the limit analysis offers some advantages: (i) reductions in the size of optimization problem; and (ii) productions of stable and accurate plasticity solution to seismic bearing capacity. In this study, we exploit the advantages of the CS-FEM (Nguyen, 2021; Nguyen and Vo-Minh, 2022b) based on the quadrilateral element mesh to revisit the upper bound solution to the undrained stability of a square tunnel. Furthermore, several analyses were conducted to calculate the seismic stability of a single square tunnel by including the horizontal seismic acceleration α_h in the simulations. This study is the extended work of Nguyen (2021) who computed the seismic stability of tunnel in homogeneous soil considering the case that the shear strength varies linearly with depth.

First, the single square tunnel problem was discretized using uniform rectangular element meshes, followed by a strain smoothing technique to approximate the displacement fields. Second, the upper bound limit analysis was cast as the second-order cone programming (SOCP) problem. This numerical procedure was adopted to assess the stability of a square tunnel that is of a width B and rests at depth H, as illustrated in Fig. 1. The collapse associated with the surcharge σ_s and the soil weight γ was used to determine the internal tunnel pressure σ_t needed to resist the collapse. The tunnel is constructed in undrained conditions where the undrained shear strength linearly increases with depth:

$$c_u(z) = c_{u0} + \rho z \tag{1}$$

where c_{u0} and $c_u(z)$ are the cohesions at the ground and the depth z, respectively.

According to Sloan and Assadi (1991), the overall stability of tunnel can be represented by two load terms, i.e. $(\sigma_s - \sigma_t)/c_{u0}$ and $\gamma B/c_{u0}$, which significantly depend on the magnitudes of H/B and $\rho B/c_{u0}$.Wilson et al. (2013) focused on the so-called stability number as below:

$$N_s = \frac{\sigma_s - \sigma_t}{c_{u0}} = f\left(\frac{H}{B}, \frac{\rho B}{c_{u0}}, \frac{\gamma B}{c_{u0}}\right) \tag{2}$$

Intensive investigations into how the undrained stability number N_s varies with the depth and the rate of changes in the undrained shear strength with depth were performed by Wilson et al. (2013) using the combination of FEM and SOCP, producing a better set of accurate collapse loads when compared with the use of FEM and LNP in the upper bound procedure (Sloan and Assadi, 1991). This research extends the work of Sloan and Assadi (1991) and Wilson et al. (2013) by giving a new (better) upper bound solution to the undrained stability number N_s using the numerical approach based on the CS-FEM and SOCP. Although the present numerical procedure is applied to resolving the stability of tunnels in purely cohesive soil, this upper bound analysis using CS-FEM is readily to estimate stability numbers for the case of highly anisotropic and heterogeneous soils which are widely encountered in the tunnel design by engineers (Krabbenhoft and Lyamin, 2015; Krabbenhoft et al., 2019). In addition, it is worth noting that the cohesion reduces as the displacement increases beyond the initial failure stage as noted by Zhang et al. (2017). This fact does not affect the magnitude of the stability number calculated using the limit theorem; however, the cohesion softening is of significance in analyzing the progressive failure of geotechnical problems, such as landslides (Skempton and Hutchinson, 1969).

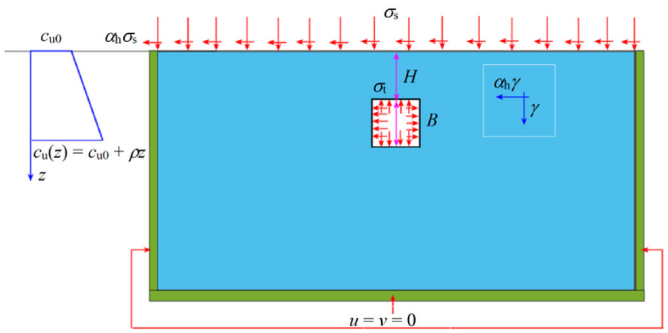

Fig. 1. Illustration of a square tunnel in the soil where the shear strength increases linearly with depth (under the static ($\alpha_h = 0$) and seismic conditions ($\alpha_h \neq 0$)).

The paper is structured as follows. In Section 2.1, we shortly present how to apply the strain smoothing technique over a single smoothing cell using uniform quadrilateral mesh. The formulation of the upper bound procedure using CS-FEM and SOCP is subsequently given in Section 2.2 to compute both the static and seismic stability of a square tunnel in heterologous soils. Several simulations using different numerical methods (both the smoothed and the standard FEMs) were conducted to prove the efficiency and accuracy of the analyses. In addition, a rich set of simulations were intensively performed in Section 3; and the numerical results are then checked against the prior contributions (Sloan and Assadi, 1991; Wilson et al., 2013). Section 4 includes some highlighting features that emerge from the present results.

2. Upper bound analysis using CS-FEM and SOCP

2.1. An overview of the CS-FEM

Herein, a brief overview of the CS-FEM to approximate the kinematically admissible displacement field is given. In the CS-FEM, a quadrilateral element can be divided into N_{cell} smaller domains inside the parent element, as illustrated in Fig. 2, leading to $\Omega = \cup_{k=1}^{N_{cell}} \Omega_k^e$. It was reported by Nguyen and Vo-Minh (2022b) that applying the strain smoothing technique to one smoothing cell can reduce variables in the mathematical optimization, while the numerical procedure is able to give very satisfactory results of the static and seismic bearing capacities of shallow strip footings. Therefore, herein we use a single smoothing cell to approximate the kinematically admissible velocity field. Smoothing strain of each cell $\dot{\boldsymbol{\varepsilon}}_{xc}$ is a function of strain of parent element, $\boldsymbol{\varepsilon}^h(x)$, and a form of distribution function, $\varphi(x)$:

$$\tilde{\dot{\boldsymbol{\varepsilon}}}_{xc} = \int_{\Omega_c^e} \boldsymbol{\varepsilon}^h(x)\varphi(x, x - x_c)\, d\Omega = \int_{\Omega_c^e} \nabla \boldsymbol{u}_x^h \varphi(x, x - x_c)\, d\Omega \tag{3}$$

One can use different types of distribution function $\varphi(x)$, which must satisfy two conditions: (i) $\varphi(x) \geq 0$; and (ii) $\int_{\Omega_c^e} \varphi(x) d\Omega = 1$.

It is noted that the compatible strain of approximate fields, $\nabla \boldsymbol{u}^h$, is approximated using $\boldsymbol{u}^h$. One can use the area of the smoothing domain Ω_e to define the distribution function:

$$\varphi(x, x - x_c) = \begin{cases} 1/A_k^{(s)} & (x \in \Omega_c^e) \\ 0 & (x \notin \Omega_c^e) \end{cases} \tag{4}$$

where $A_k^{(s)} = \int_{\Omega_c^e} d\Omega$ is the area of the cell Ω_c^e.

If one applies the divergence theorem, then the smoothing strain can be written as

$$\tilde{\dot{\boldsymbol{\varepsilon}}}_{xc} = \frac{1}{A_c} \int_{\Omega_c^e} \nabla \boldsymbol{u}^h(x) d\Omega = \oint \boldsymbol{n}_x \boldsymbol{u}^h(x) d\Gamma_c \tag{5}$$

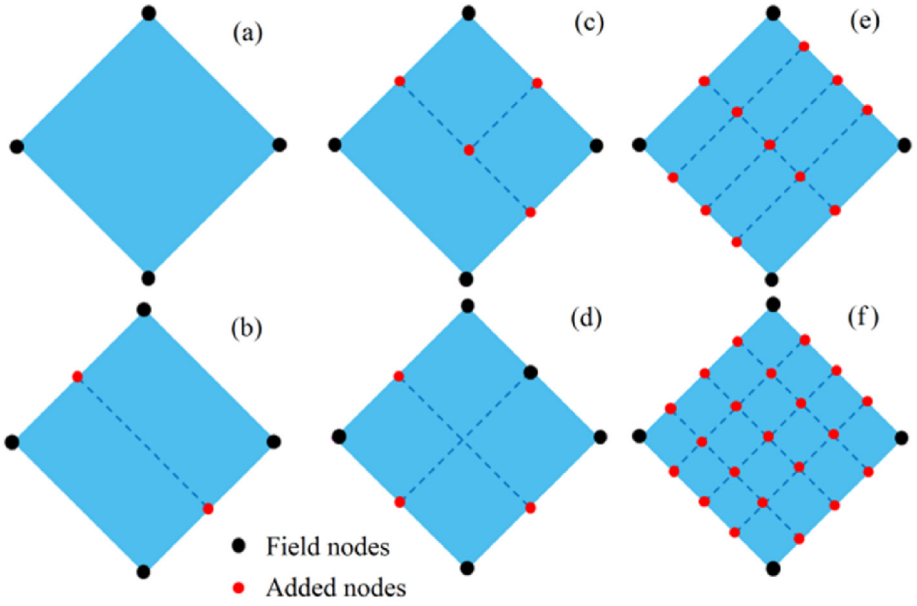

Fig. 2. Division of a quadrilateral element into smaller smoothing cells (SSC): (a) SSC = 1; (b) SSC = 2; (c) SSC = 3; (d) SSC = 4; (e) SSC = 8; and (f) SSC = 16.

where Γ_c is the boundary of smoothing domain as illustrated in Fig. 3, and the normal vector $\boldsymbol{n}_x$ is expressed as

$$\boldsymbol{n}_x = \begin{bmatrix} n_x & 0 \\ 0 & n_y \\ n_y & n_x \end{bmatrix} \tag{6}$$

Therefore, the smoothing strain rate can be calculated as $\tilde{\dot{\boldsymbol{\varepsilon}}}_{xc} = \dot{\boldsymbol{B}}\dot{\boldsymbol{d}}$, in which $\boldsymbol{d}$ is the displacement vector of the nodes associated with the quadrilateral element, and $\dot{\boldsymbol{B}}$ is the strain-displacement matrix defined by

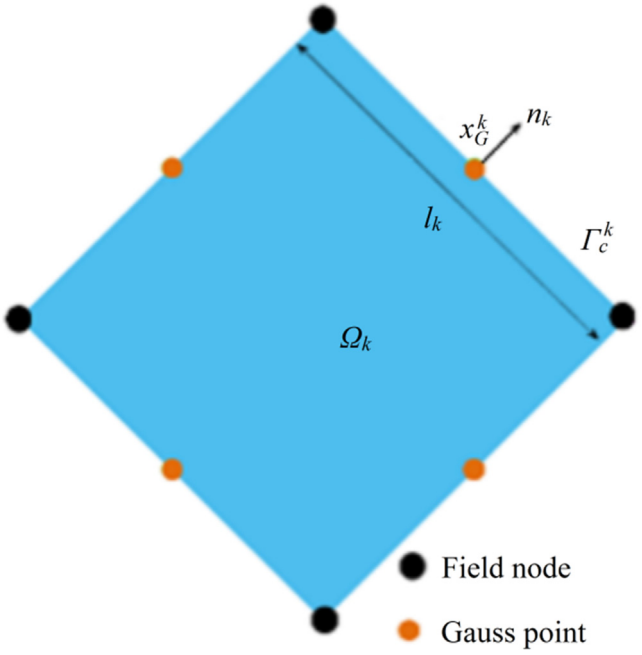

Fig. 3. The smoothing domain using a single smoothing cell Ω_k with the Gauss point x_G^k of boundary segment Γ_c^k.

$$\dot{\tilde{\mathbf{B}}} = \begin{bmatrix} \tilde{N}_{1,x}^{x_c} & 0 & \cdots & \tilde{N}_{n,x}^{x_c} & 0 \\ 0 & \tilde{N}_{1,y}^{x_c} & \cdots & 0 & \tilde{N}_{n,y}^{x_c} \\ \tilde{N}_{1,y}^{x_c} & \tilde{N}_{1,x}^{x_c} & \cdots & \tilde{N}_{n,y}^{x_c} & \tilde{N}_{n,x}^{x_c} \end{bmatrix} \tag{7}$$

$$\tilde{N}_{I,x}^{x_c} = \frac{1}{A_k^{(s)}} \oint N_{I,x} \boldsymbol{n}(x) \mathrm{d}\Gamma_c \tag{8}$$

where $\tilde{N}_{I,x}^{x_c}$ is the smoothed version of shape function derivative $N_{I,x}^{x_c}$, and $\boldsymbol{n}(x)$ is the normal vector associated with the boundary segment Γ_c^k. It should be noted that all computations were performed using the Gauss point. Referring to Fig. 3, x_G^k is the Gauss point of boundary segment Γ_c which has length l_k and outward surface normal vector $\boldsymbol{n}_k$.

2.2. Establishment of upper bound optimization problems as SOCP

It is well known that the structure will collapse if and only if there exists a kinematically admissible displacement field $\dot{\boldsymbol{u}} \in \boldsymbol{U}$, where $\boldsymbol{U}$ is a space of kinematically admissible velocity field, thus we have

$$W_{\mathrm{int}}(\dot{\boldsymbol{\varepsilon}}^{\mathrm{p}}) = D(\dot{\boldsymbol{\varepsilon}}^{\mathrm{p}}) < \beta^{+} W_{\mathrm{ext}}(\dot{\boldsymbol{u}}) + W_{\mathrm{ext}}^{0}(\dot{\boldsymbol{u}}) \tag{9}$$

where $W_{\mathrm{int}}(\dot{\boldsymbol{\varepsilon}}^{\mathrm{p}}) = D(\dot{\boldsymbol{\varepsilon}}^{\mathrm{p}})$ is the internal plastic dissipation; β^{+} is the collapse load multiplier; $W_{\mathrm{ext}}^{0}(\dot{\boldsymbol{u}})$ is the work done by any additional loads ($\boldsymbol{f}_0$ and $\boldsymbol{g}_0$) not subjected to the multiplier; and $W_{\mathrm{ext}}(\dot{\boldsymbol{u}})$ is the external work rate of a rigid-perfectly plastic body of area $\Omega \in \boldsymbol{R}^2$ with boundary Γ, which is subjected to body force $\boldsymbol{f}$ and surface traction $\boldsymbol{g}$:

$$W_{\mathrm{int}}(\dot{\boldsymbol{\varepsilon}}^{\mathrm{p}}) = D(\dot{\boldsymbol{\varepsilon}}^{\mathrm{p}}) = \int_{\Omega} \boldsymbol{f}^{\mathrm{T}} \dot{\boldsymbol{u}} \mathrm{d}\Omega + \int_{\Gamma} \boldsymbol{g}^{\mathrm{T}} \dot{\boldsymbol{u}} \mathrm{d}\Gamma \tag{10}$$

The strain rate can be expressed as

$$\dot{\boldsymbol{\varepsilon}}^{\mathrm{p}} = \left[\dot{\varepsilon}_{xx}^{\mathrm{p}} \;\; \dot{\varepsilon}_{yy}^{\mathrm{p}} \;\; \dot{\gamma}_{xy}^{\mathrm{p}}\right]^{\mathrm{T}} = \nabla \dot{\boldsymbol{u}} \tag{11}$$

The space of kinematically admissible velocity field $\boldsymbol{U}$ is denoted by

$$\boldsymbol{U} = \left\{ \dot{\boldsymbol{u}} \in \left(H^1(\Omega)\right)^2,\ \dot{\boldsymbol{u}} = \overline{\dot{\boldsymbol{u}}} \text{ on } S_{\dot{\boldsymbol{u}}} \right\} \tag{12}$$

If we define $C = \{\dot{\boldsymbol{u}} \in \boldsymbol{U} | W_{\text{ext}}(\dot{\boldsymbol{u}}) = 1\}$, the limit analysis problem is based on the kinematical theorem to determine the collapse load multiplier β^+ yielding the following optimization problem:

$$\beta^+ = \max\{\exists \boldsymbol{\sigma} \in \sum | W_{\text{int}}(\boldsymbol{\sigma}, \dot{\boldsymbol{u}}) = \alpha W_{\text{ext}}(\dot{\boldsymbol{u}}), \forall \dot{\boldsymbol{u}} \in \boldsymbol{U}\} = \min_{\dot{\boldsymbol{u}} \in \boldsymbol{U}} D_{\text{p}}(\dot{\boldsymbol{u}}) \quad (\dot{\boldsymbol{u}} = 0\ (\text{on } S_{\boldsymbol{u}}),\ W_{\text{ext}}(\dot{\boldsymbol{u}}) = 1) \tag{13}$$

For plane strain problems based on the Mohr–Coulomb failure criterion, Makrodimopoulos and Martin (2007) proposed the internal plastic dissipation equation as follows:

$$D_{\text{p}}(\dot{\boldsymbol{u}}) = c \cos\phi \int_{\Omega} \sqrt{\left(\tilde{\dot{\varepsilon}}_{xx}^{\text{pi}} - \tilde{\dot{\varepsilon}}_{yy}^{\text{pi}}\right)^2 + \left(\tilde{\dot{\gamma}}_{xy}^{\text{pi}}\right)^2} \mathrm{d}\Omega \tag{14}$$

where c and ϕ are the cohesion and friction angle of the soil, respectively.

For an associated flow rule, the plastic strain rate vector is given by

$$\dot{\boldsymbol{\varepsilon}}^{\text{p}} = \mu \frac{\partial \psi(\boldsymbol{\sigma})}{\partial \boldsymbol{\sigma}} \tag{15}$$

where μ is a non-negative plastic multiplier, and the Mohr–Coulomb yield function $\psi(\boldsymbol{\sigma})$ can be expressed in the form of stress components as

$$\psi(\boldsymbol{\sigma}) = \sqrt{(\sigma_{xx} - \sigma)_{yy}^2 + 4\tau_{xy}^2} + (\sigma_{xx} + \sigma_{yy})\sin\phi - 2c\cos\phi \tag{16}$$

We aim to form the upper bound solutions as conic quadratic optimization in the quadratic form as noted by Zhang et al. (2019):

$$\kappa_q = \left\{ \boldsymbol{x} \in \boldsymbol{R}^m \middle| x_1^2 \geq \sqrt{x_2^2 + x_3^2 + \cdots + x_n^2} \right\} \tag{17}$$

where $\boldsymbol{x} = (x_1, x_2, \ldots, x_n)^{\text{T}}$ is the vector consisting of the field variables, and κ_q is a tensorial product of second-order cones (i.e. $\kappa_q = \kappa_1 \kappa_2 \cdots \kappa_n$). To formulate the collapse load multiplier β^+ as the quadratic form, we need to introduce χ_i such that $\|\zeta_i\| \leq \chi_i$, in which

$$\boldsymbol{\zeta}_i = \begin{bmatrix} \zeta_i^2 \\ \zeta_i^2 \end{bmatrix} = \begin{bmatrix} \tilde{\dot{\varepsilon}}_{xx}^{\text{pi}} - \tilde{\dot{\varepsilon}}_{yy}^{\text{pi}} \\ \tilde{\dot{\gamma}}_{xy}^{\text{pi}} \end{bmatrix} \tag{18}$$

Using CS-FEM, the problem is discretized by Ncell smoothing domains. The smoothed strain rate $\tilde{\dot{\boldsymbol{\varepsilon}}}$ can be calculated from Eq. (3). The upper bound limit analysis for plane strain problems using the Mohr–Coulomb failure criterion can be written as

$$\begin{aligned} \beta^+ &= \min\left(\sum_{i=1}^{N_{\text{cell}}} cA_i \cos\phi \sqrt{\left(\tilde{\dot{\varepsilon}}_{xx}^{\text{pi}} - \tilde{\dot{\varepsilon}}_{yy}^{\text{pi}}\right)^2 + \left(\tilde{\dot{\gamma}}_{xy}^{\text{pi}}\right)^2} - W_{\text{ext}}^0(\dot{\boldsymbol{u}}) \right) \\ &= \min\left(\sum_{i=1}^{N_{\text{cell}}} cA_i \chi_i \cos\phi - W_{\text{ext}}^0(\dot{\boldsymbol{u}}) \right) \end{aligned} \tag{19a}$$

subject to

$$\left.\begin{aligned} &\dot{\boldsymbol{u}} = 0\ (\text{on } \Gamma_{\boldsymbol{u}}) \\ &W_{\text{ext}}(\dot{\boldsymbol{u}}) = 1 \\ &\tilde{\dot{\varepsilon}}_{xx}^{\text{pi}} + \tilde{\dot{\varepsilon}}_{yy}^{\text{pi}} = \chi_i \sin\phi \\ &\chi_i \geq \sqrt{\left(\tilde{\dot{\varepsilon}}_{xx}^{\text{pi}} - \tilde{\dot{\varepsilon}}_{yy}^{\text{pi}}\right)^2 + \left(\tilde{\dot{\gamma}}_{xy}^{\text{pi}}\right)^2}\ (i = 1, 2, \ldots, N_{\text{cell}}) \end{aligned}\right\} \tag{19b}$$

where A_i is the area of the smoothing domain of cell i, and the collapse load multiplier β^+ is the static or seismic bearing capacity factor in this study. The last constraint in Eq. (19b) is expressed in the conic form. As a result, the conic interior-point optimizer of the academic MOSEK package (MOSEK ApS, 2015) is used to solve this problem. The upper bound using the CS-FEM has been written using the Matlab language. The computations were performed on the Dell precision 5520 (Intel(R) Xeon(R) CPU E3-1505 M v5 2.80 GHz, 32 Gb RAM) in the Window 10 Pro; and the combination of CS-FEM and SOCP in the upper bound analysis has been written in the Matlab language. In short, the whole procedure of numerical procedure using CS-FEM and SOCP can be depicted in Fig. 4 that shows algorithms to implement into the code.

3. Limit analysis of stability of a square tunnel

Having presented a combination of CS-FEM and SOCP in the previous section, we used this numerical procedure to calculate the so-called $N_{\text{s}} = (\sigma_{\text{s}} - \sigma_{\text{t}})/c_{\text{u0}}$ for various H/B ratios. As shown in Fig. 5, only half of a square tunnel was considered in the analyses. The boundary conditions were set in the simulations as given in Fig. 5 due to the geometry of symmetry. Displacement conditions along the boundary were set in the simulations as illustrated in Fig. 5, where the displacement condition $u = v = 0$ was installed

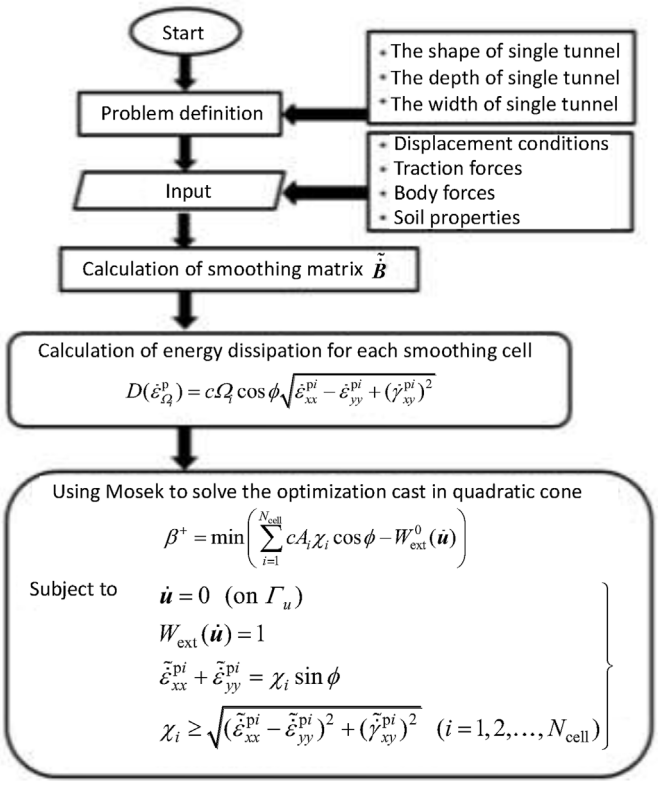

Fig. 4. Illustration of upper bound limit analysis using CS-FEM and SOCP.

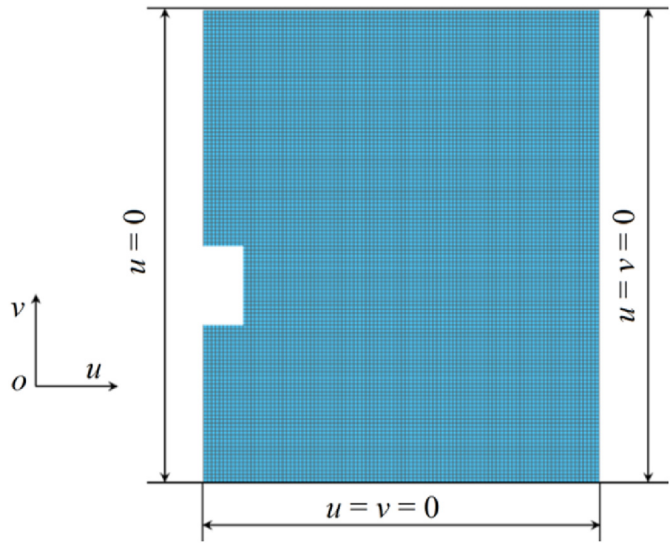

Fig. 5. Representative quadrilateral element mesh for $H/B = 3$, showing boundary conditions.

Table 1
The static stability of a square tunnel for the case of $H/B = 1$, $\rho B/c_{u0} = 0$, and $\gamma B/c_{u0} = 0$.

S_{dof}	N_e	N_{var}	CPU (s)	N_s
312	128	696	0.11	3.41
1002	450	2352	0.16	3.24
3802	1800	9202	0.33	3.10
8402	4200	20,552	1.03	3.05
14,802	7200	36,402	2.11	1.98

along the bottom and the right of domain considered and the horizontal displacements $u = 0$ was set along the left of the domain of analyses. It is noted that all domains should be large enough to remove the effect of boundary conditions on the numerical solutions.

In order to prove the accuracy and efficiency of the current numerical approach using CS-FEM, we consider the case of $H/B = 1$, $\rho B/c_{u0} = 0$, and $\gamma B/c_{u0} = 0$. The total number of variables N_{var}, the number of elements N_e, degree of freedoms, S_{dof}, CPU time, and the values of the static stability number are listed in Table 1. The lower and upper bound solutions to the stability number given by Wilson et al. (2013) are $N_s = 1.94$ and $N_s = 1.98$, respectively. While this study used only about more than 7000 elements, the present results are equal to the finite element upper bound limit analysis given by Wilson et al. (2013) who used a significantly larger number of elements in the analyses (i.e. about 100,000 elements with discontinuity elements). The validation of this numerical approach for the collapse loads under seismic conditions has been presented by Nguyen and Vo-Minh (2022b), and the interested readers are referred to this reference for more details on the comparison of the use of CS-FEM and other FEMs in the limit analysis. This confirms the effectiveness and the accuracy of the present analysis for calculation of the stability of a square tunnel.

It is worth noting that the collapse of the tunnel occurs at constant volume with presented simulations using the constrained conditions as stated by Wilson et al. (2013) (see Eq. (19b)). The dimensionless stability is quantified by setting the surcharge to zero, i.e. $\sigma_s = 0$. A rich set of simulations were performed by the present approach for various cases of dimensionless parameters (H/B, $\rho B/c_{u0}$, and $\gamma B/c_{u0}$). We varied H/B from 1 to 10 to investigate how the depth of a square tunnel influences the stability. For each tunnel depth, the soil unit weight ($\gamma B/c_{u0}$) was varied from 0 to 5, in which $\gamma B/c_{u0} = 0$ is analogous to the case of tunnel in the weightless soil. In addition, the undrained shear strength varies linearly with depth, representing the strength parameter ($\rho B/c_{u0}$) of the soil changing between 0 and 1. The dimensionless parameter N_s is computed and reported in the Appendix, along with a comparison of the present results with two bounds on the undrained stability given by Sloan and Assadi (1991) and Wilson et al. (2013), as shown in Figs. 6–10. Overall, the numerical results are better than both upper bounds given in Wilson et al. (2013) and the upper bound solutions reported in Sloan and Assadi (1991). For all cases of analyses, the stability numbers obtained using CS-FEM are lower than those given by the prior contributions (Sloan and Assadi, 1991; Wilson et al., 2013). As expected, as the shear strength increases, the stability number increases for all cases of analysis of the weightless soil ($\gamma B/c_{u0} = 0$) and the soil considering its weight ($\gamma B/c_{u0} = 1 - 5$). As noted by Wilson et al. (2013), a negative value of the stability number indicates that the application of a compressive normal stress to the tunnel face is required to prevent the failure from occurring. On the other hand, a positive value of N_s implies that the tunnel itself is safe from failure. Numerical results reveal that, for a tunnel of moderate depth, N_s values decrease

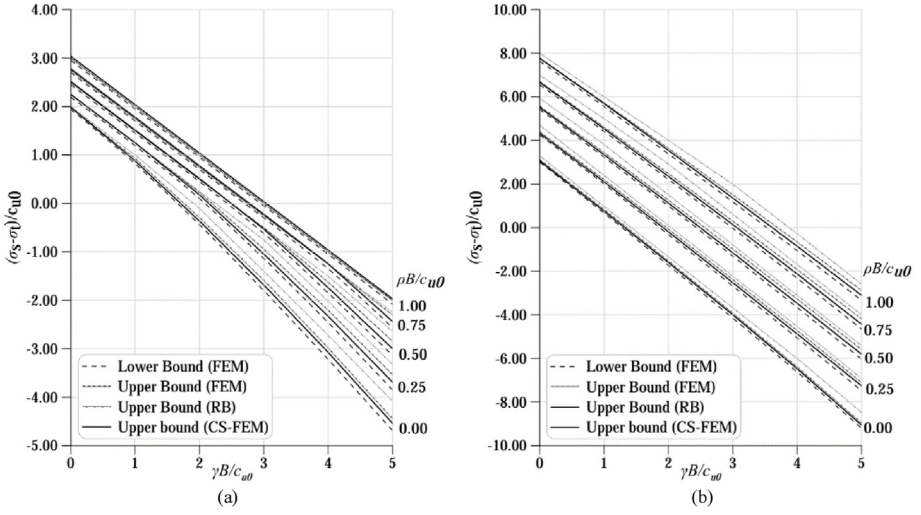

Fig. 6. Comparison of the stability of a square tunnel obtained in the present study and those given by Wilson et al. (2013) for: (a) $H/B = 1$; and (b) $H/B = 2$.

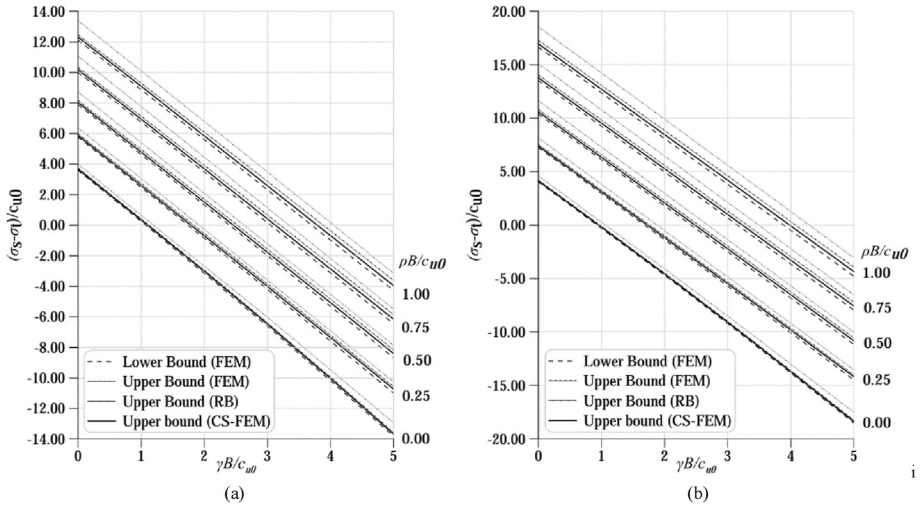

Fig. 7. Comparison of the stability of a square tunnel obtained in the present study and those given by Wilson et al. (2013) for: (a) $H/B = 3$; and (b) $H/B = 4$.

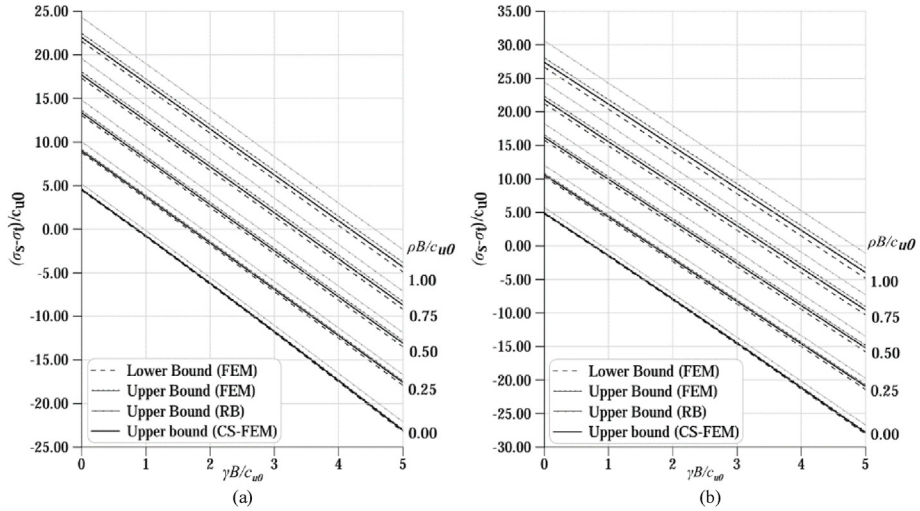

Fig. 8. Comparison of the stability of a square tunnel obtained in the present study and those given by Wilson et al. (2013) for: (a) $H/B = 5$; and (b) $H/B = 6$.

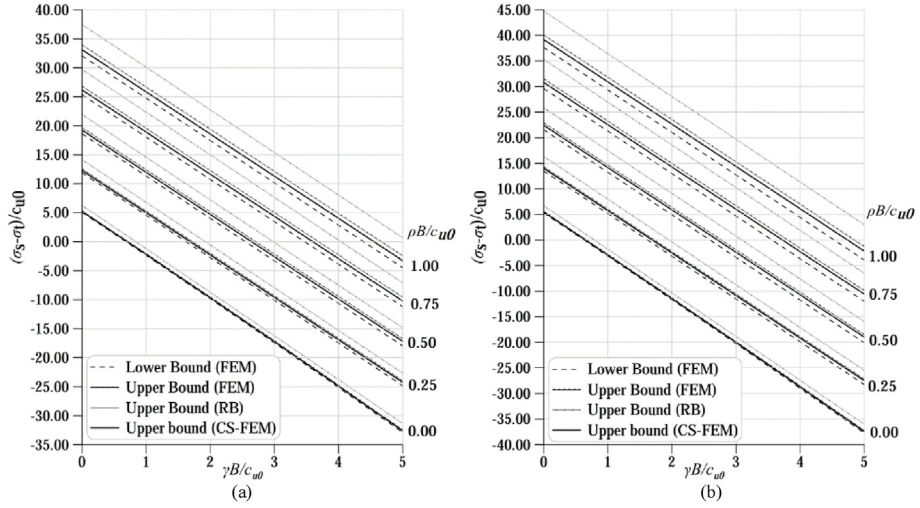

Fig. 9. Comparison of the stability of a square tunnel obtained in the present study and those given by Wilson et al. (2013) for: (a) $H/B = 7$; and (b) $H/B = 8$.

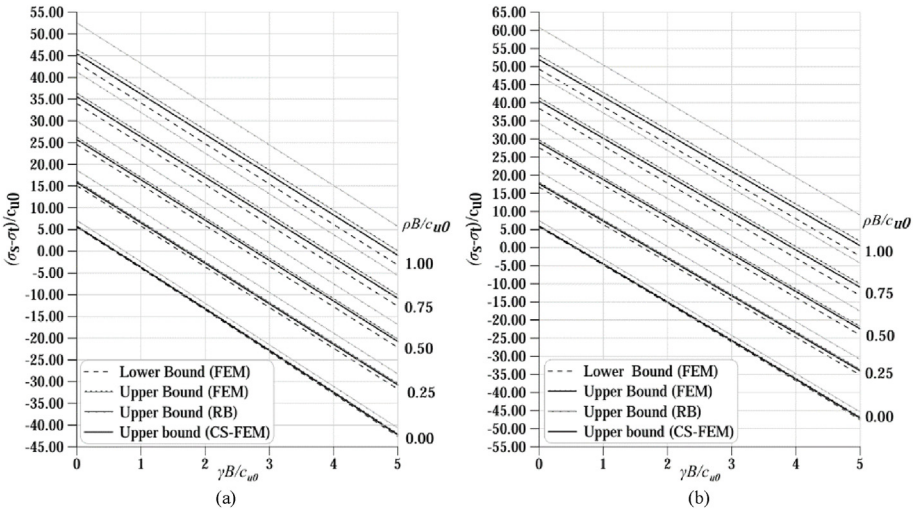

Fig. 10. Comparison of the stability of a square tunnel obtained in the present study and those given by Wilson et al. (2013) for: (a) $H/B = 9$; and (b) $H/B = 10$.

significantly as $\gamma B/c_{u0}$ increases, meaning that the supporting forces are needed to maintain the stability of the tunnel.

For practical design, three rigid block mechanisms (Wilson et al., 2013) are useful to calculate the stability number of a single square tunnel. It was reported by Wilson et al. (2013) that the mechanism a is suitable for estimations of the stability number for a shallow tunnel where the failure occurs on the top (i.e. the roof) of tunnel (Fig. 11). Numerical results are found in an excellent agreement with the trapdoor style mechanism (the mechanism a) for the shallow tunnel, as shown in Fig. 11. When the ratio H/B increases, the use of the mechanisms b and c are likely to successfully capture the failure mechanism which takes place on the wall and the floor of tunnel. Figs. 12 and 13 show the numerical results of failure mechanism for deeper tunnels, agreeing very well with the mechanisms b and c proposed by Wilson et al. (2013). In particular, Fig. 12 shows the comparison of failure mechanism with the mechanism b for $H/B = 1$, $\rho B/c_{u0} = 0.25$, and $\gamma B/c_{u0} = 3$, in which both types of failure occur on the wall of the tunnel. For deeper tunnels, the failure domain becomes deeper, as shown in Fig. 13, where the failure occurs beneath the floor of tunnel. This observation provides a check on applications of the rigid block mechanism c for prediction of the undrained stability of a deeper tunnel.

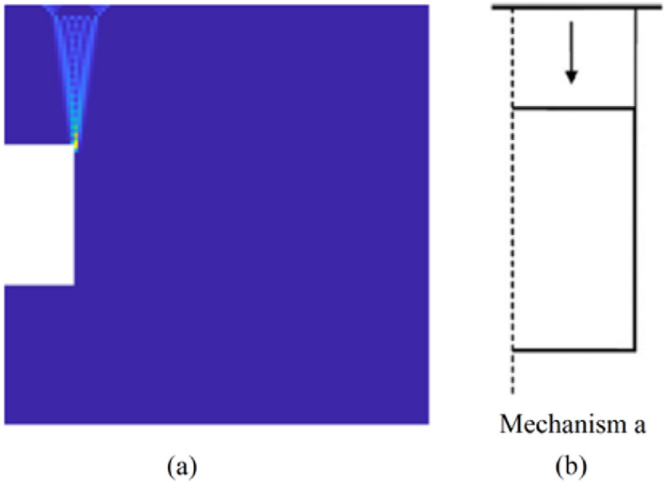

Fig. 11. A comparison of the power dissipation intensity and the rigid block mechanism for $H/B = 1$, $\rho B/c_{u0} = 0$, and $\gamma B/c_{u0} = 0$: (a) This study; and (b) The mechanism a given in Wilson et al. (2013).

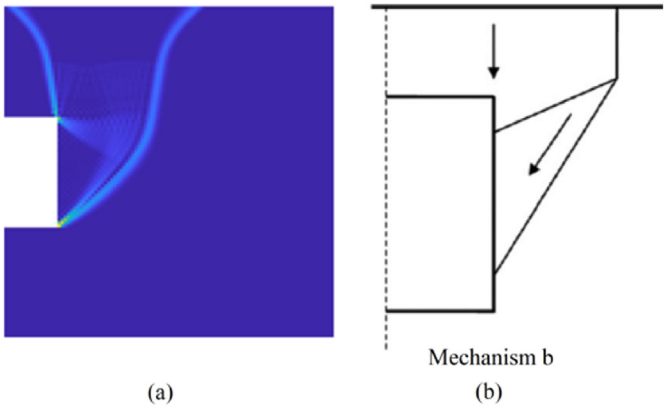

Fig. 12. A comparison of the power dissipation intensity and the rigid block mechanism for $H/B = 1$, $\rho B/c_{u0} = 0.25$, and $\gamma B/c_{u0} = 3$: (a) This study; and (b) The mechanism b given in Wilson et al. (2013).

In addition, the magnitude of the stability number for the homogeneous soil obtained by the present analysis is better than both upper bound solutions given in Sloan and Assadi (1991) and Wilson et al. (2013). It was revealed by Wilson et al. (2013) that the failure pattern is strongly dependent upon the H/B and $\gamma B/c_{u0}$ ratios. A comparison of power dissipation intensity with the work of Wilson et al. (2013) for $H/B = 1$, $\rho B/c_{u0} = 0$, and $\gamma B/c_{u0} = 0$ is given in Fig. 14, confirming that the trapdoor mechanism successfully captures the failure pattern for shallow tunnel in the soil with a low unit weight. Numerical results confirm that the failure pattern of a shallow tunnel with $H/B \leq 1$ in a weightless soil remains unchanged, having a trapdoor mechanism when the ratio $\rho B/c_{u0}$ varies. However, this feature does not hold for a shallow circle tunnel as reported by Wilson et al. (2011). In addition, a rigid block mechanism (b) seems to be suitable for capturing the failure mode for a shallow tunnel ($H/B \leq 1$) in the soil considering its weight.

Figs. 15–18 show the comparison of the failure mechanism obtained in this study with those given by Wilson et al. (2013) when the depth of tunnels increases, indicating that the failure shapes derived from both numerical approaches are in an excellent agreement. The expansion of the domain of failure mechanism in conjunction with the depth of failure zone provides a check on observations given in Wilson et al. (2013). In addition, as the $\rho B/c_{u0}$

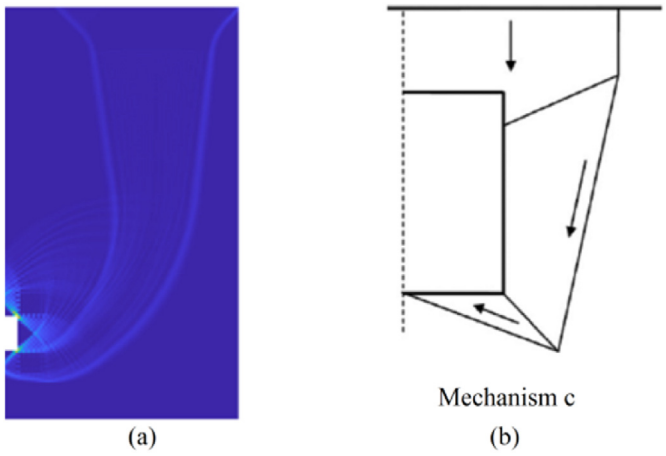

Fig. 13. A comparison of the power dissipation intensity and the rigid block mechanism for $H/B = 9$, $\rho B/c_{u0} = 0$, and $\gamma B/c_{u0} = 0$: (a) This study; and (b) The mechanism c given inWilson et al. (2013).

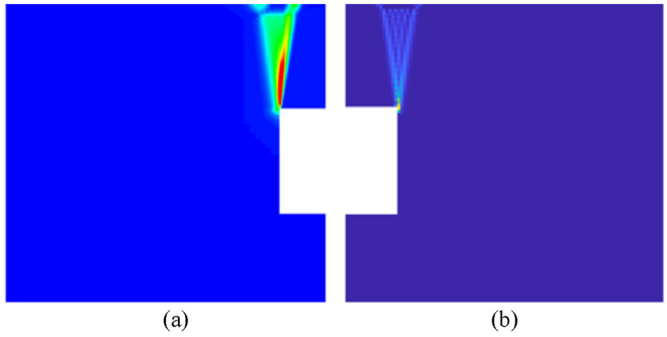

Fig. 14. Comparison of power dissipation intensity with the work of Wilson et al. (2013) for $H/B = 1$, $\rho B/c_{u0} = 0$, and $\gamma B/c_{u0} = 0$: (a) Wilson et al. (2013); and (b) CS-FEM.

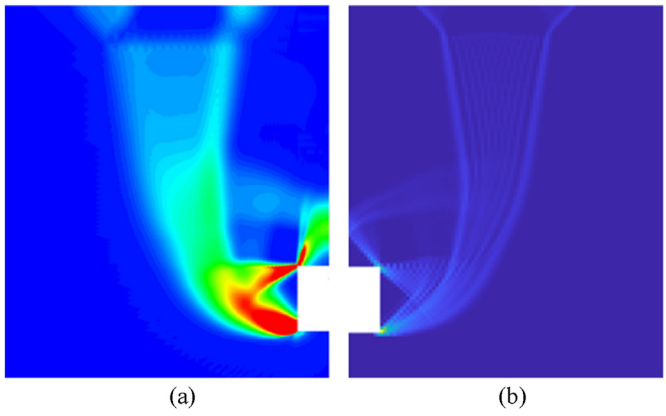

Fig. 15. Comparison of the power dissipation intensity for $H/B = 4$, $\rho B/c_{u0} = 0$, and $\gamma B/c_{u0} = 1$: (a) Wilson et al. (2013); and (b) CS-FEM.

ratio increases, the failure becomes more localized when comparing the failure domain in Fig. 15 with that in Fig. 16 for a tunnel of moderate depth ($H/B = 4$). The effect of $\rho B/c_{u0}$ on characteristics of failure pattern becomes significant as the H/B ratio increases, as illustrated in Figs. 17 and 18 for $\gamma B/c_{u0} = 1$. Although the failure pattern becomes narrower with increasing values of $\rho B/c_{u0}$, the value of stability number increases, as reported in the Appendix.

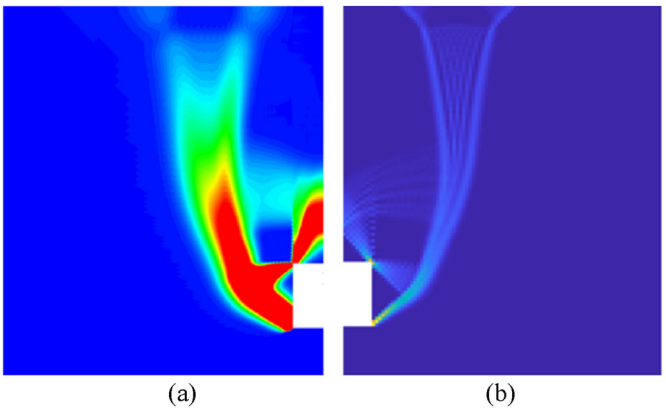

Fig. 16. Comparison of the power dissipation intensity for $H/B = 4$, $\rho B/c_{u0} = 1$, and $\gamma B/c_{u0} = 1$: (a) Wilson et al. (2013); and (b) CS-FEM.

To facilitate the practical use of tunnel design by engineers, we propose a new expression to compute the undrained stability of a square tunnel in terms of the three dimensionless parameters, i.e. H/B, $\rho B/c_{u0}$, and $\gamma B/c_{u0}$. It is shown in Figs. 6–10 where the so-called $N_s = (\sigma_s - \sigma_t)/c_{u0}$ is proportional to the $\gamma B/c_{u0}$ ratio in a linear manner, leading to a formulation of the stability number that is the function of N_0 and N_γ:

$$N_s = N_0 + \frac{\gamma B}{c_{u0}} N_\gamma = N_0 + \frac{\gamma B}{c_{u0}} \left(\zeta \frac{\rho B}{c_{u0}} + \psi \right) \tag{20}$$

where N_0 and N_γ are the stability factors which account for the weightless soil and the soil considering weight, respectively. It is noted that two parameters, ζ and ψ, are quantified using the appropriate regression over the numerical results. Fitting the whole set of numerical results listed in the Appendix for the case of $\gamma B/c_{u0} = 0$ gives a new expression for N_0 which is a function of H/B and $\rho B/c_{u0}$:

$$N_0 = 1.442 \left(\frac{\rho B}{c_{u0}} \frac{H}{B} + 1.293 \right) \ln \left(2.316 \frac{H}{B} + 0.253 \right) \tag{21}$$

In order to generate an expression for the factor N_γ, various options using parametric curve-fitting techniques to fit Eqs. (20) and (21) are adopted until an appropriate expression can be achieved to match quite closely with the present solution. The following is the parametric equation for the stability factor accounting for the soil weight:

$$N_\gamma = \frac{-0.142}{\tan \left[10446.5 (H/B)^{-1} + 4.446 H \big/ B \right]} \frac{\rho B}{c_{u0}} \frac{H}{B} - 0.77 \ln \frac{H}{B} - \frac{H}{B} \tag{22}$$

where the two parameters ζ and ψ (Eq. (20)) are the functions of H/B. A check on the newly proposed equation was made by comparing the values of N_s derived from Eq. (20) and the equation proposed by Wilson et al. (2013), along with the average values of both lower and upper bounds on the N_s values. As shown in Fig. 19, the new parametric equation gives much better values of the undrained stability of a circular tunnel than that formulation given by Wilson et al. (2013). For the weightless soil, the values of N_s are equivalent to the case of N_0. It can be observed from Fig. 19a that there are no differences between the values obtained by the new equation and the average values of two bounds given by Wilson et al. (2013) for the homogeneous soil. In particular, both equations give almost the same values of the stability number for $\rho B/c_{u0} \leq 0.25$. However, it is

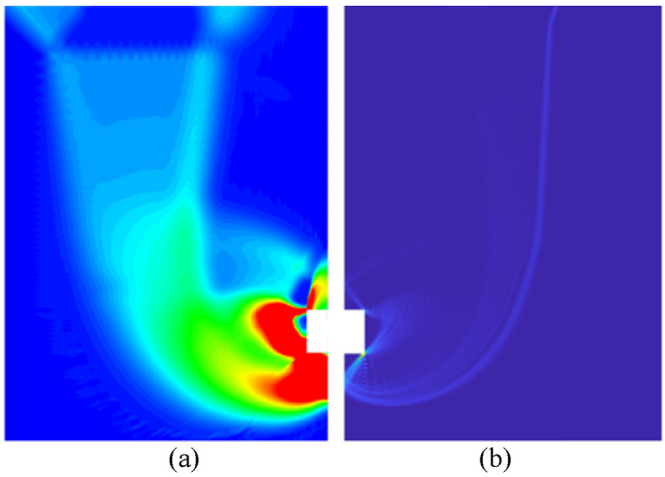

Fig. 17. Comparison of the power dissipation intensity for $H/B = 7$, $\rho B/c_{u0} = 0$, and $\gamma B/c_{u0} = 3$: (a) Wilson et al. (2013); and (b) CS-FEM.

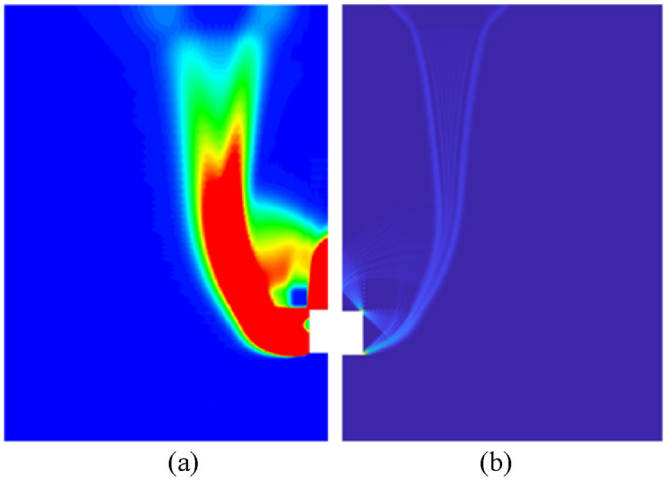

Fig. 18. Comparison of the power dissipation intensity for $H/B = 7$, $\rho B/c_{u0} = 1$, and $\gamma B/c_{u0} = 3$: (a) Wilson et al. (2013); and (b) CS-FEM.

shown that the new equation derived from the present study better predicts the undrained stability for $\rho B/c_{u0} \geq 0.5$. Similar behavior is obtained for the cases of $\gamma B/c_{u0} = 1$ for $\rho B/c_{u0} \leq 0.25$. On the other hand, when $\rho B/c_{u0}$ increases, the present formulation predicts better values (i.e. closer to the average values of two bounds on N_s) of the undrained stability of a square tunnel when compared with that given by Wilson et al. (2013). For the soil considering weight, when $\gamma B/c_{u0}$ varies from 1 to 5, the N_s values obtained using the new expression are much closer to the average values of the two bound solutions, indicating that the new formulation gives better values of the stability number than that given by Wilson et al. (2013). It is shown in Fig. 19b–f that for deeper tunnels, the new closed-form expression of N_s is much better than that given by Wilson et al. (2013) when utilized to predict the stability number. In short, for both the weightless soil and the soil considering weight, the new equation derived from the present study acts as a better means to interpret the undrained stability of a square tunnel. Although the new equation proposed for predicting the undrained stability number gives a better fit to the exact values of the stability number for the purely cohesive soil, there are still trivial discrepancies between the predicted results from the current expression and the average results for highly anisotropic and heterogeneous soils (i.e. with large values of $\rho B/c_{u0}$). These predictions can be applicable in the practical use by engineers.

Apart from calculation of static stability of a square tunnel, several simulations were carried out to estimate the seismic stability of a square tunnel. Herein, an extension of the work carried out by Nguyen (2021), who assessed the effect of seismic loading on the tunnel stability for a homogeneous soil (i.e. $\rho B/c_{u0} = 0$), was made by considering the case that the undrained shear strength linearly increases with depth. It is shown from Fig. 20 that under the static condition, the failure mechanism is symmetric; however, the plastic mechanism becomes asymmetric with the increasing value of horizontal seismic acceleration. This leads to a reduction in the magnitude of the stability number.

In order to assess the effect of seismic loadings on the undrained stability of tunnel in the soil where the shear strain increases linearly with depth, several simulations were performed for two values of depth ratio, $H/B = 1$ and $H/B = 3$. We varied α_h from 0 to 0.5, taking into account the weightless soil ($\gamma B/c_{u0} = 0$) and the soil considering weight ($\gamma B/c_{u0} = 1$) in the analyses for each depth. In this case, the so-called seismic stability number is defined as

$$N_{sE}^{\alpha_h} = g\left(\alpha_h, \frac{H}{B}, \frac{\rho B}{c_{u0}}, \frac{\gamma B}{c_{u0}}\right) \tag{23}$$

The seismic stability number $N_{sE}^{\alpha_h}$ described in Eq. (23) and its static counterpart N_s shown in Eq. (2), can be related using the following expression:

$$N_{sE}^{\alpha_h} = e_{sE}^{\alpha_h} N_s \tag{24}$$

where the corrective coefficient $e_{sE}^{\alpha_h}$ represents the reduction in the value of the stability number due to seismic effects. The numerical results are listed in Table 2 for $H/B = 1$ and Tables 3–5 for $H/B = 3$, revealing that $N_{sE}^{\alpha_h}$ decreases as α_h increases. However, the seismic stability number depends on the $\gamma B/c_{u0}$ and $\rho B/c_{u0}$ ratios in a highly complex manner. Referring to Figs. 21 and 22, the corrective coefficient becomes larger as the unit weight of soil mass increases; however, the degree of the reduction in the seismic stability number tends to reduce for the case of the homogeneous soil where there is no changes in the shear strength with depth. In addition, the corrective factors drop significantly when the tunnel depth increases. This striking feature holds for tunnels in highly heterogeneous soil (i.e. the ratio $\rho B/c_{u0}$ increases). It is evident that soil inertia significantly affects the seismic stability number of a square tunnel and at a high value of α_h, the seismic stability number drops to the same value, regardless of the value of the ratio $\rho B/c_{u0}$ used in the analyses.

4. Conclusions

A CS-FEM is presented to calculate the undrained stability of a square tunnel, eliminating volumetric locking issues and the singularity associated with the Mohr–Coulomb model. A series of computations was performed to calculate the undrained stability of a square tunnel in the soil where the undrained shear strength varies with depth in a linear manner. Numerical results are in excellent agreement with prior contributions (Sloan and Assadi, 1991; Wilson et al., 2013), giving new upper bounds on the undrained stability that are better than the results given by Sloan and Assadi (1991) and Wilson et al. (2013) for deeper tunnels. As $\gamma B/c_{u0}$ increases, the numerical results of $N_s = (\sigma_s - \sigma_t)/c_{u0}$ become significantly improved. Failure mechanisms obtained agree very well with the rigid block mechanisms used in Sloan and Assadi (1991) and the kinematic failure patterns used in the upper bound FEM, which changes with increasing depth values. Several

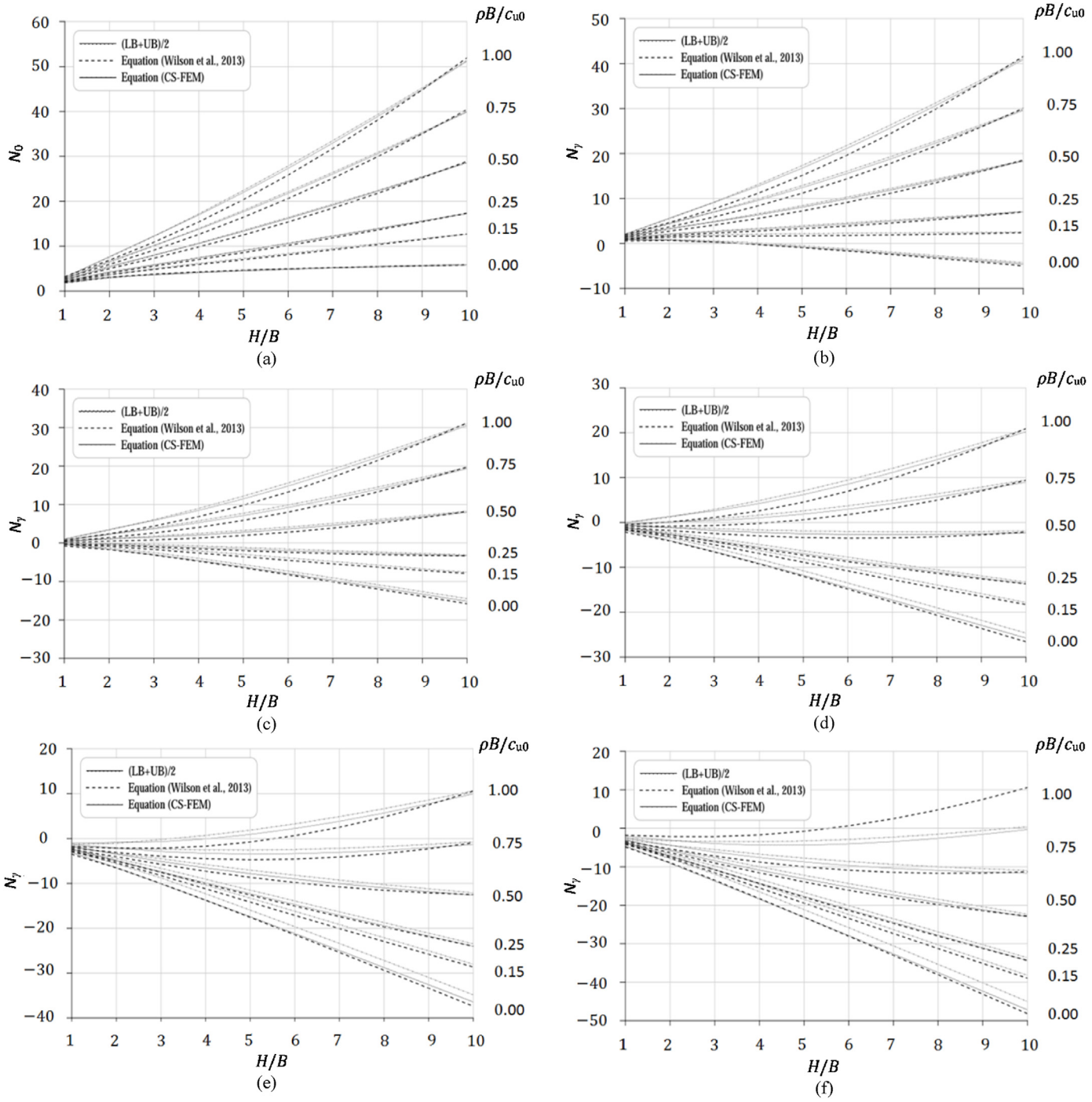

Fig. 19. Comparison of the N_0 and N_γ values obtained by the newly proposed expression with those given by Wilson et al. (2013): (a) N_0 for $\gamma B/c_{u0} = 0$; (b) N_γ for $\gamma B/c_{u0} = 1$; (c) N_γ for $\gamma B/c_{u0} = 2$; (d) N_γ for $\gamma B/c_{u0} = 3$; (e) N_γ for $\gamma B/c_{u0} = 4$; and (f) N_γ for $\gamma B/c_{u0} = 5$. LB and UB denote the lower and upper bounds, respectively.

stability tables and charts are given for the practical use of tunnel design, along with the newly proposed approximate equation for calculating the undrained stability of a square tunnel in the soil where the shear strength increase with depth in a linear form.

Several computational performances have been conducted to calculate the seismic stability number. The results confirm that the seismic stability number reduces as α_h increases for both cases of the weightless soil and the soil considering weight. The corrective coefficient was quantified to link the static stability number to its seismic counterpart. The numerical results reveal that the corrective coefficient e_{sE} becomes larger with increasing values of soil unit weight. In addition, the magnitude of corrective coefficient increases as the $\gamma B/c_{u0}$ ratio reduces; however, this coefficient drops significantly for deep tunnels (i.e. the H/B ratio increases). This upper bound numerical procedure is readily to extend to three-dimensional (3D) limit analysis of tunnel stability in highly anisotropic and heterogeneous soils which are often encountered in tunnel designs by geotechnical engineers.

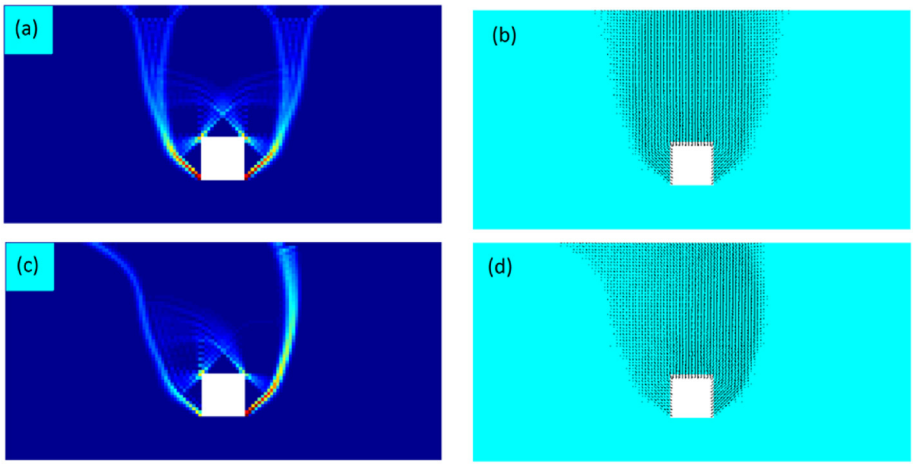

Fig. 20. Displacement field and power dissipation intensity for the static and seismic stability of a square tunnel with $\gamma B/c_{u0} = 3$, $\rho B/c_{u0} = 3$, and $H/B = 3$: (a) power dissipation intensity for $N_s = 5.87$ and $\alpha_h = 0$; (b) Displacement field for $N_s = 5.87$ and $\alpha_h = 0$; (c) Power dissipation intensity for $N_s = 5.72$ and $\alpha_h = 0.1$; and (d) Displacement field for $N_s = 5.72$ and $\alpha_h = 0$.

Table 2
The seismic stability number and the corrective coeffcient of a square tunnel for $H/B = 1$, and $\gamma B/c_{u0} = 0$ and 1, with $A = \rho B/c_{u0}$.

α_h	$N_{sE}^{\alpha_h}$ for $\gamma B/c_{u0} = 0$			$e_{sE}^{\alpha_h}$ for $\gamma B/c_{u0} = 0$			$N_{sE}^{\alpha_h}$ for $\gamma B/c_{u0} = 1$			$e_{sE}^{\alpha_h}$ for $\gamma B/c_{u0} = 1$		
	$A = 1$	$A = 0.5$	$A = 0$	$A = 1$	$A = 0.5$	$A = 0$	$A = 1$	$A = 0.5$	$A = 0$	$A = 1$	$A = 0.5$	$A = 0$
0	3.24	2.65	2.04	1	1	1	2.57	1.97	1.31	1	1	1
0.1	3.16	2.6	1.99	0.98	0.98	0.97	2.53	1.96	1.29	0.98	0.99	0.99
0.2	2.99	2.48	1.87	0.92	0.94	0.92	2.43	1.9	1.25	0.95	0.96	0.96
0.3	2.75	2.31	1.74	0.85	0.87	0.85	2.3	1.82	1.21	0.9	0.92	0.92
0.4	2.47	2.1	1.61	0.76	0.79	0.79	2.15	1.73	1.16	0.84	0.87	0.89
0.5	2.1	1.88	1.48	0.65	0.71	0.72	1.98	1.62	1.12	0.77	0.82	0.85

Table 3
The seismic stability number and the corrective coeffcient of a square tunnel for $H/B = 3$, and $\gamma B/c_{u0} = 0$ and 1, with $A = \rho B/c_{u0}$.

α_h	$N_{sE}^{\alpha_h}$ for $\gamma B/c_{u0} = 0$			$e_{sE}^{\alpha_h}$ for $\gamma B/c_{u0} = 0$			$N_{sE}^{\alpha_h}$ for $\gamma B/c_{u0} = 1$			$e_{sE}^{\alpha_h}$ for $\gamma B/c_{u0} = 1$		
	$A = 1$	$A = 0.5$	$A = 0$	$A = 1$	$A = 0.5$	$A = 0$	$A = 1$	$A = 0.5$	$A = 0$	$A = 1$	$A = 0.5$	$A = 0$
0	12.36	8.06	3.68	1	1	1	10.22	5.90	1.48	1	1	1
0.1	10.52	7.64	3.55	0.85	0.95	0.97	9.68	5.69	1.46	0.95	0.96	0.99
0.2	5.26	5.13	3.31	0.43	0.64	0.9	5.29	5.17	1.43	0.52	0.88	0.97
0.3	3.51	3.42	3.01	0.28	0.42	0.82	3.54	3.46	1.38	0.35	0.59	0.93
0.4	2.63	2.57	2.5	0.21	0.32	0.68	2.66	2.6	1.32	0.26	0.44	0.9
0.5	2.1	2.05	2	0.17	0.25	0.54	2.14	2.09	1.26	0.21	0.35	0.85

Table 4
The seismic stability number and the corrective coeffcient of a square tunnel for $H/B = 3$, and $\gamma B/c_{u0} = 2$ and 3, with $A = \rho B/c_{u0}$.

α_h	$N_{sE}^{\alpha_h}$ for $\gamma B/c_{u0} = 2$			$e_{sE}^{\alpha_h}$ for $\gamma B/c_{u0} = 2$			$N_{sE}^{\alpha_h}$ for $\gamma B/c_{u0} = 3$			$e_{sE}^{\alpha_h}$ for $\gamma B/c_{u0} = 3$		
	$A = 1$	$A = 0.5$	$A = 0$	$A = 1$	$A = 0.5$	$A = 0$	$A = 1$	$A = 0.5$	$A = 0$	$A = 1$	$A = 0.5$	$A = 0$
0	8.06	3.73	1.54	1	1	1	5.9	23.01	25.13	1	1	1
0.1	7.76	3.66	1.52	0.96	0.98	0.99	5.76	11.09	11.62	0.98	0.48	0.46
0.2	5.33	3.51	1.47	0.66	0.94	0.96	5.33	5.58	5.86	0.90	0.24	0.23
0.3	3.57	3.33	1.4	0.44	0.89	0.91	3.61	3.74	3.94	0.61	0.16	0.16
0.4	2.7	2.63	1.3	0.33	0.71	0.85	2.7	2.82	2.98	0.46	0.12	0.12
0.5	2.17	2.12	1.16	0.27	0.57	0.75	2.2	2.3	2.4	0.37	0.1	0.1

Table 5
The seismic stability number and the corrective coeffcient of a square tunnel for $H/B = 3$, and $\gamma B/c_{u0} = 4$ and 5, with $A = \rho B/c_{u0}$.

α_h	$N_{sE}^{\alpha_h}$ for $\gamma B/c_{u0} = 4$			$e_{sE}^{\alpha_h}$ for $\gamma B/c_{u0} = 4$			$N_{sE}^{\alpha_h}$ for $\gamma B/c_{u0} = 5$			$e_{sE}^{\alpha_h}$ for $\gamma B/c_{u0} = 5$		
	$A = 1$	$A = 2$	$A = 3$	$A = 1$	$A = 2$	$A = 3$	$A = 1$	$A = 2$	$A = 3$	$A = 1$	$A = 2$	$A = 3$
0	3.73	12.36	20.88	1	1	1	10.2	18.75	35.7	1	1	1
0.1	3.68	11.15	11.65	0.99	0.9	0.56	9.87	11.69	12.69	0.97	0.62	0.36
0.2	3.55	5.64	5.89	0.95	0.46	0.28	5.68	5.93	6.43	0.56	0.32	0.18
0.3	3.35	3.81	3.97	0.9	0.31	0.19	3.84	4.01	4.34	0.38	0.21	0.12
0.4	2.76	2.89	3.01	0.74	0.23	0.14	2.92	3.05	3.3	0.29	0.16	0.09
0.5	2.24	2.34	2.44	0.6	0.19	0.12	2.37	2.47	2.67	0.23	0.13	0.07

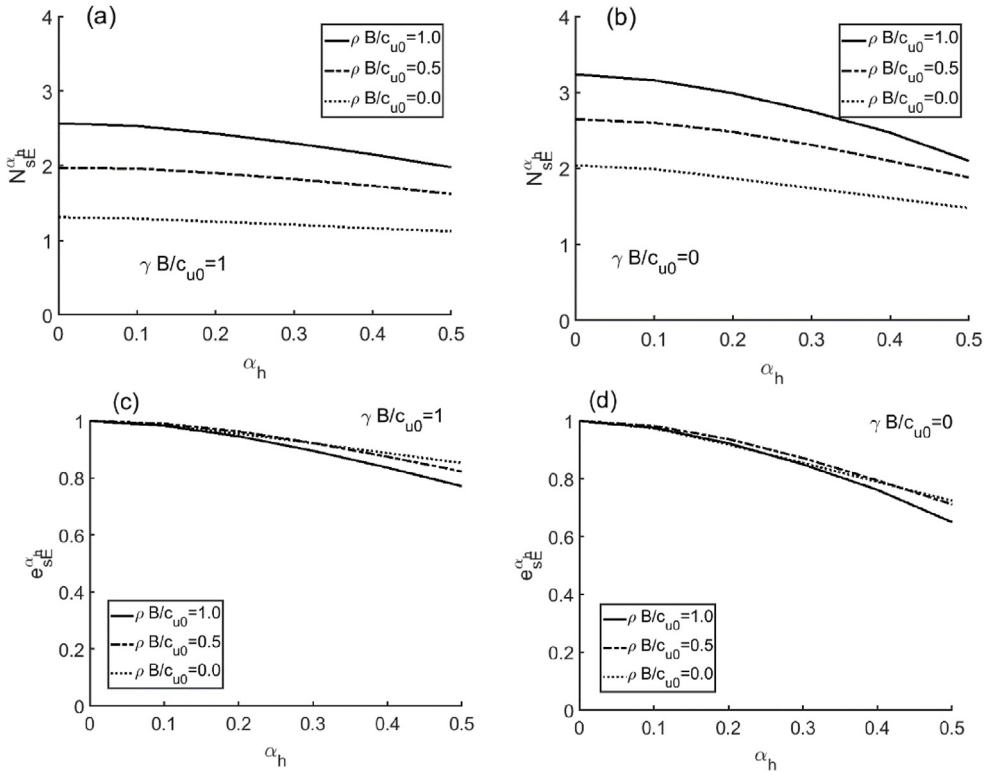

Fig. 21. The seismic stability numberand the corrective coeffcient for $H/B = 1$: (a) $N_{sE}^{\alpha_h}$ for $\gamma B/c_{u0} = 1$; (b) $N_{sE}^{\alpha_h}$ for $\gamma B/c_{u0} = 0$; (c) $e_{sE}^{\alpha_h}$ for $\gamma B/c_{u0} = 1$; and (d) $e_{sE}^{\alpha_h}$ for $\gamma B/\ c_{u0} = 0$.

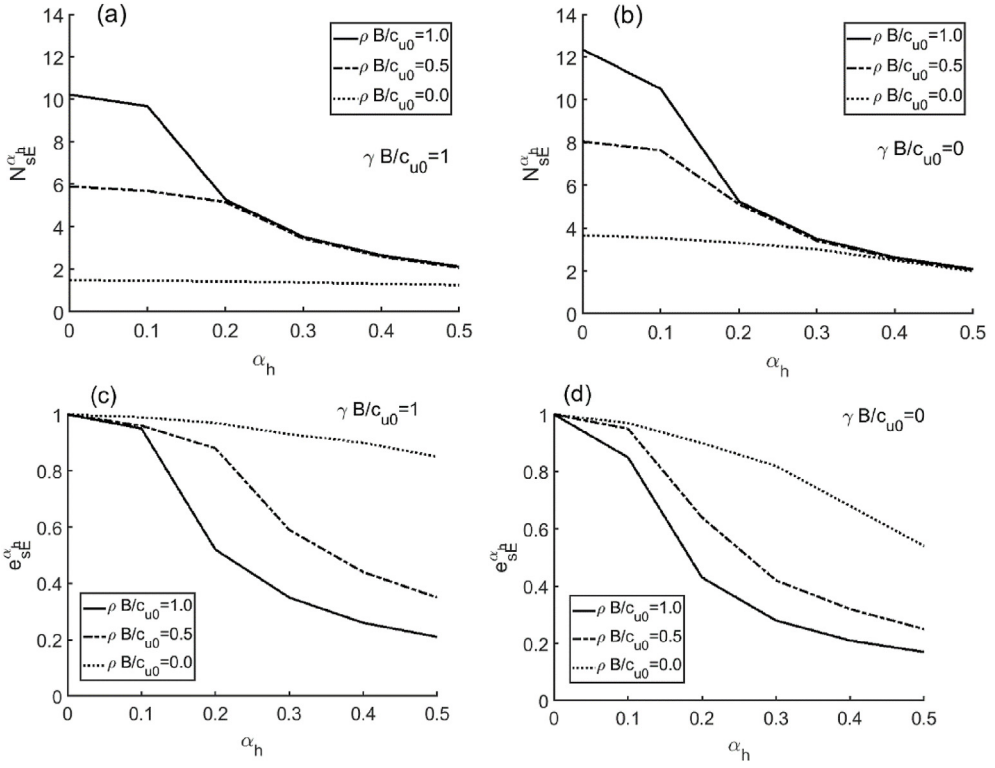

Fig. 22. The seismic stability number and the corrective coeffcient for $H/B = 3$: (a) $N_{sE}^{\alpha_h}$ for $\gamma B/c_{u0} = 1$; (b) $N_{sE}^{\alpha_h}$ for $\gamma B/c_{u0} = 0$; (c) $e_{sE}^{\alpha_h}$ for $\gamma B/c_{u0} = 1$; and (d) $e_{sE}^{\alpha_h}$ for $\gamma B/\ c_{u0} = 0$.

Declaration of competing interest

The authors declare that they have no known competing financial interests or personal relationships that could have appeared to influence the work reported in this paper.

Acknowledgements

This is part of the TPS project. The first author is grateful to a Vied-Newton PhD scholarship and a Dixon scholarship from Imperial College London, UK, for supporting his studies at Imperial College London. He is also indebted to the Dean's Fund from Imperial College London for financial support (2017–2020).

References

Krabbenhoft, K., Galindo-Torres, S.A., Zhang, X., Krabbenhøft, J., 2019. AUS: anisotropic undrained shear strength model for clays. Int. J. Numer. Anal. Methods GeoMech. 43 (17), 2652–2666.

Krabbenhoft, K., Lyamin, A.V., 2015. Generalised Tresca criterion for undrained total stress analysis. Géotech. Lett. 5 (4), 313–317.

Makrodimopoulos, A., Martin, C.M., 2007. Upper bound limit analysis using simplex strain elements and second-order cone programming. Int. J. Numer. Anal. Methods GeoMech. 31 (6), 835–865.

Meng, J., Zhang, X., Huang, J., Tang, H., Mattsson, H., Laue, J., 2020. A smoothed finite element method using second-order cone programming. Comput. Geotech. 123, 103547.

MOSEK ApS, 2015. MOSEK Optimization Toolbox for MATLAB. MOSEK ApS, Copenhagen, Denmark.

Nguyen, H.C., 2021. Upper bound analysis of seismic stability of tunnels using cell-based smoothed finite element. In: Elshafie, M.Z.E.B., Viggiani, G.M.B., Mair, R.J. (Eds.), Geotechnical Aspects of Underground Construction in Soft Ground. CRC Press, London, UK.

Nguyen, H.C., Vo-Minh, T., 2022a. The use of the node-based smoothed finite element method to estimate static and seismic bearing capacities of shallow strip footings. J. Rock Mech. Geotech. Eng. 14 (1), 180–196.

Nguyen, H.C., Vo-Minh, T., 2022b. Calculation of seismic bearing capacity of shallow strip footings using the cell-based smoothed finite element. Acta Geotech. https://doi.org/10.1007/s11440-021-01421-4.

Skempton, A., Hutchinson, J., 1969. Stability of natural slopes and embankment foundations. In: Proceedings of the 7th International Conference on Soil Mechanics and Foundation Engineering. State-of-art Volume, Mexico City, Mexico, pp. 291–340.

Sloan, S.W., Assadi, A., 1991. Undrained stability of a square tunnel in a soil whose strength increases linearly with depth. Comput. Geotech. 12 (4), 321–346.

Vo-Minh, T., Nguyen-Son, L., 2021. A stable node-based smoothed finite element method for stability analysis of two circular tunnels at different depths in cohesive-frictional soils. Comput. Geotech. 129, 103865.

Wilson, D.W., Abbo, A.J., Sloan, S.W., Lyamin, A.V., 2011. Undrained stability of a circular tunnel where the shear strength increases linearly with depth. Can. Geotech. J. 48, 1328–1342.

Wilson, D.W., Abbo, A.J., Sloan, S.W., Lyamin, A.V., 2013. Undrained stability of a square tunnel where the shear strength increases linearly with depth. Comput. Geotech. 49, 314–325.

Zhang, X., Oñate, E., Torres, S.A.G., Bleyer, J., Krabbenhoft, K., 2019. A unified Lagrangian formulation for solid and fluid dynamics and its possibility for modelling submarine landslides and their consequences. Comput. Methods Appl. Mech. Eng. 343, 314–338.

Zhang, X., Sheng, D., Sloan, S.W., Bleyer, J., 2017. Lagrangian modelling of large deformation induced by progressive failure of sensitive clays with elasto-viscoplasticity. Int. J. Numer. Methods Eng. 112 (8), 963–989.

Dr. H.C. Nguyen obtained his PhD degree in Civil Engineering at Imperial College London, UK. During his PhD, Dr. Nguyen was awarded the Dean's Fund from Imperial College London (2017–2020). After his PhD studies, Dr. Nguyen worked as a postdoctoral research associate in Computational Geomechanics group at the University of Liverpool, UK. He developed advanced numerical procedures using the 3D smoothed particle FEM to Cam–Clay plasticity solutions for geomechanical problems.